Saturn's northern auroras as observed using the Hubble Space Telescope

J.D. Nichols [a,*], S.V. Badman [b], E.J. Bunce [a], J.T. Clarke [c], S.W.H. Cowley [a], G.J. Hunt [a], G. Provan [a]

[a] Department of Physics and Astronomy, University of Leicester, Leicester, UK
[b] Department of Physics, Lancaster University, Lancaster, UK
[c] Center for Space Physics, Boston University, Boston, MA 02215, USA

ARTICLE INFO

ABSTRACT

We discuss the features of Saturn's northern FUV auroras as observed during a program of Hubble Space Telescope observations which executed over 2011–2013 and culminated, along with Cassini observations, in a comprehensive multi-spectral observing campaign. Our 2011–2013 observations of the northern aurora are also compared with those from our 2007–2008 observation of the southern aurora. We show that the variety of morphologies of the northern auroras is broadly consistent with the southern, and determine the statistical equatorward and poleward boundary locations. We find that our boundaries are overall consistent with previous observations, although a modest poleward displacement of the poleward boundaries is due to the increased prevalence of poleward auroral patches in the noon and afternoon sectors during this program, likely due to the solar wind interaction. We also show that the northern auroral oval oscillates with the northern planetary period oscillation (PPO) phase in an elongated ellipse with semi-major axis ∼1.6° oriented along the post-dawn/post-dusk direction. We further show that the northern auroras exhibit dawn-side brightenings at zero northern magnetic PPO phase, although there is mixed evidence of auroral emissions fixed in the rotating frame of the northern PPO current system, such that overall the dependence of the auroras on northern magnetic phase is somewhat weak.

1. Introduction

Saturn's southern ultraviolet (UV) auroras have been observed extensively over the past decade using high-sensitivity instruments onboard the Hubble Space Telescope (HST) such as the Space Telescope Imaging Spectrograph (STIS) and the Advanced Camera for Surveys (ACS) (e.g. Gérard et al., 2004; Grodent et al., 2005; Clarke et al., 2009). The southern auroral emission consists of a ∼2° wide 'oval' of radius ∼10–20° co-latitude (Badman et al., 2006; Clarke et al., 2009; Carbary, 2012). The oval is generally brighter on the dawn side, and patches of emission are observed to slide along the oval at ∼20–70% of corotation (Grodent et al., 2005; Meredith et al., 2013; Lamy et al., 2013). Transient, bright features are occasionally observed both poleward and equatorward of the oval (Gérard et al., 2004, 2005; Meredith et al., 2013; Radioti et al., 2013; Meredith et al., 2014), and separate emission has been observed ∼3° equatorward of the main oval on the nightside (Grodent et al., 2010). This collection of features is thought to be the manifestation of a number of different magnetospheric phenomena, such as sub-rotation of magnetospheric plasma, plasma injections and day- and night-side reconnection. The morphology of the auroras has also been observed to change dramatically following the arrival of an interplanetary shock, with bright aurora expanding significantly toward the pole on the dawn side (Crary et al., 2005; Clarke et al., 2005, 2009), a form associated with the compression-induced collapse of the tail (Cowley et al., 2005; Nichols et al., 2014). The quiet time oval also exhibits an oscillation of amplitude ∼1° along the prenoon–premidnight meridian with a period consistent with that of the Saturn Kilometric Radiation (SKR) (Nichols et al., 2008, 2010b), a phenomenon that has been shown to be associated with planetary-period oscillations (PPOs) in the magnetic field (Provan et al., 2009), the high latitude plasmapause-like boundary (Gurnett et al., 2011) and the location of the field-aligned currents as measured in situ by Cassini (Bunce et al., 2014). The brightness of the oval is also modulated at the PPO period, with the brighter dawn-side auroras pulsing in phase with the SKR, whilst the less intense dusk-side auroras oscillate in anti-phase, implicating a weak rotational modulation of the auroral field-aligned currents with a strong superposed dawnside strobe-like enhancement (Nichols et al., 2010a). Such behaviour was later confirmed using magnetic field and radio observations (Andrews et al., 2011; Lamy, 2011).

* Corresponding author.
  E-mail address: jdn4@le.ac.uk (J.D. Nichols).

However, prior to the program of observations discussed in this paper, HST had only previously been able to view the planet's northern auroras from extremely oblique viewing angles due to the planet's seasons (Nichols et al., 2009), such that the above results relate to southern hemisphere data obtained during southern summer, and comparable images of the northern auroras had not been yet obtained. Using the equinoctial images Nichols et al. (2009) were, however, able to show that Saturn's northern and southern auroras often simultaneously differ significantly in size, intensity and morphology. For example, the northern oval was observed to be typically ∼1.5° smaller than the southern, ascribed to the stronger internal magnetic field in the north (e.g. Dougherty et al., 2005), and individual blobs of emission do not always have a conjugate counterpart. The latter phenomenon was shown by Meredith et al. (2013) to be consistent with even modes of ULF field line resonances producing hemispherically anti-symmetric field-aligned currents, leading to auroral emission in one hemisphere with no conjugate counterpart. Meredith et al. (2014) went on to examine the HST images of Saturn's northern auroras obtained in 2011 and 2012 as part of the program discussed in this paper, with reference to prevailing upstream conditions in the interplanetary medium as observed by Cassini. They found that the patches and arcs observed just poleward of the main oval near noon are present during intervals of northward IMF, thus favouring low-latitude dayside reconnection. None of these patches were observed when the IMF was southward, although a very high latitude form observed during such an interval was associated with lobe reconnection on open field lines, as discussed previously by Bunce et al. (2005) and Gérard et al. (2005). Recently, auroral storms observed in 2013 during the HST program discussed in this paper were discussed by Nichols et al. (2014), who reported bursts of emission moving quickly toward the morningside on the poleward edge of the expanded auroras. These bursts, somewhat reminiscent of terrestrial poleward boundary intensifications and coincident with a ∼1° poleward motion of the poleward boundary, were associated with the ongoing rapid closure of lobe flux in the tail. A later, more evolved, storm form, i.e. a region of bright, poleward-expanded emission, was shown by those authors to map to the trailing region of an energetic neutral atom enhancement observed by the magnetospheric imaging instrument (MIMI) onboard Cassini. This emission was thus associated with the upward field-aligned continuity current flowing into the trailing region of the eastward-directed partial ring current imaged by MIMI.

The planet's northern auroras have also been observed using the Ultraviolet Imaging Spectrograph (UVIS) and the Visual and Infrared Mapping Spectrometer (VIMS) instruments onboard the Cassini orbiter, results from which have revealed a brightening associated with plasma energisation in the nightside sector (Mitchell et al., 2009), and small-scale features such as the Enceladus footprint (Pryor et al., 2011), auroral spots near the main oval (Grodent et al., 2011), bifurcations in the auroral oval in the noon to dusk sector (Radioti et al., 2011) possibly associated with dayside reconnection, features associated with injections (Radioti et al., 2013), and tail dipolarisations (Jackman et al., 2013). A number of similar structures have been observed in the infrared (IR) (Badman et al., 2012a). However, the 'pseudo-images' obtained using UVIS are obtained by slewing the instrument's slit over the auroral region, a process which results in the last pixel being obtained tens of minutes after the first, such that caution must be exercised when comparing the results with the exposures obtained by HST. Thus, while individual aspects of the northern auroras as observed during the present HST program and by UVIS have been previously presented, an overview of the statistics and morphology of Saturn's northern auroras as observed using FUV imaging with HST remains to be presented. We discuss the recent 3-year program of HST/ACS observations of Saturn's northern auroras, which executed over 2011–2013 and culminated in the 2013 multi-wavelength program which is the subject of the present issue. Specifically, we discuss the morphologies observed, the overall statistics of the auroral location and modulation of the emission with PPO phase.

2. HST images

Over 2011–2013, a total of 570 images of Saturn's northern UV auroras were obtained near opposition using the Solar Blind Channel (SBC) of the ACS from sub-Earth latitudes increasing from ∼8.5° in 2011 to ∼18.6° in 2013. The observing intervals were 1–9 April 2011, 28 March–6 April 2012, and 5 April–22 May 2013, and the program comprised 5 orbits in 2011, 10 in 2012, and 15 in 2013, with nineteen individual exposures obtained during each orbit. The reduction of such ACS/SBC images of Saturn's auroras has been extensively discussed previously (see e.g. Clarke et al., 2009; Nichols et al., 2009), such that here we simply note that in each orbit nineteen 100s exposures were obtained using the ACS/SBC detector, which is a 1024×1024 Multi-Anode Microchannel Array with a field of view of 35×31 arcsec^2. Images were mostly obtained using the F115LP and F125LP longpass filters, which have cut-off wavelengths of 115 and 125 nm respectively, such that the latter admits H_2 Lyman and Werner bands, while the former also includes H Lyman-α emission. Exposures have been co-added in groups of 5 (F125LP), 5 (F115LP), 4 (F115LP), and 5 (F125LP) in each orbit in order to increase the signal-to-noise at the cost of ∼5° blurring at the central meridian longitude (CML) for corotating features. A few exposures each year were obtained using the F145LP and F165LP filters, which block the auroral emissions and are thus used for background subtraction as discussed by the above-cited works. The units were converted from counts to kR (where 1 kR represents a source flux of 10^9 ph cm^{-2} s^{-1} radiating into 4π steradians) of H_2 emission using the conversion factors 1 kR $= 2.05 \times 10^{-3}$ and 1.20×10^{-3} counts s^{-1} for the F115LP and F125LP filters, respectively (Gustin et al., 2012), and the images were projected onto a planetocentric latitude–longitude grid assuming an emission altitude of 1100 km above the 1 bar reference spheroid, in conformity with the observed peak in the emission (Gérard et al., 2009).

3. Analysis

3.1. Morphology

We first discuss the variety of auroral morphologies observed in the north over this program. All the images obtained in the program are available in movies (files sat11.mov, sat12.mov and sat13.mov for images obtained in 2011, 2012, and 2013, respectively) in the Supplementary Material (SM), which show both the unprojected and projected views of the images. Representative images from each year are displayed in Figs. 1 (2011, 2012) and 2 (2013), which show Lambert Equal Area Azimuthal projections of the images as viewed from above the north pole, with the central meridian longitude (CML) oriented toward the bottom. Note that, as discussed above, a number of features of the 2011 and 2012 images have been discussed by Meredith et al. (2014), and we initially briefly review these images here. Although, particularly for 2011, the sub-Earth latitude permitted only a view of the dayside auroras, it is first apparent that the northern auroras exhibit a variety of morphologies, similar to those in the south. Hence, the quiet-time oval associated with interplanetary rarefaction regions is evident in all years, e.g. in Figs. 1a, e and i, and 2c, brighter in the dawn than in the dusk, and in some cases the
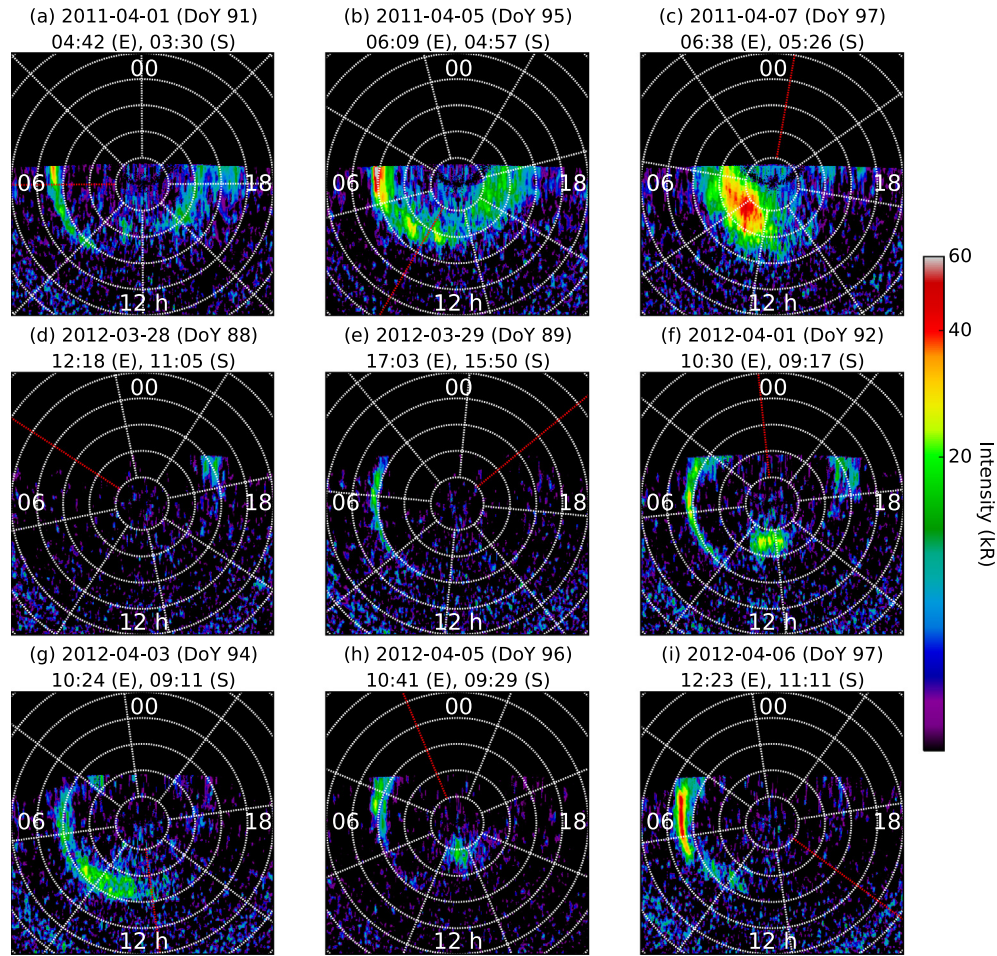
Fig. 1. Figure showing representative images obtained during 2011 and 2012. Each image is labelled with the date and time of the exposure at Earth (E) and corrected for one-way light travel time from Saturn (S). Each image is shown on a Lambert Equal Area Azimuthal projection, with noon oriented to the bottom. A $5° \times 45°$ latitude–longitude grid is overlaid by the grey dotted lines, and the direction of $\Psi_{mag\,S} = 0°$ is shown by the red line. The intensities are shown on a log-scale, saturated at 30 kR. (For interpretation of the references to colour in this figure legend, the reader is referred to the web version of this article.)

auroras are so quiet that there is barely any emission at all, as in Figs. 1d and 2b. Auroral storms comprising bright, dawnside poleward expansions associated with interplanetary compressions are also evident, as shown in Figs. 1c and 2a, g, and h, and discussed further in Nichols et al. (2014). Particularly prominent throughout the program were forms poleward of the main oval in the noon and afternoon sectors, shown by Meredith et al. (2014) to be present during intervals of northward IMF. Examples are shown in Figs. 1f and h, and 2c, e, f, and i. In the case of the form observed on day 113 in 2013, shown in Fig. 2e and f, the patch moved poleward by ∼2° over the course of the ∼50 min HST observing interval. Such motion of emissions near the cusp at Earth have been traditionally associated with flux tube motion following low-latitude dayside reconnection. The poleward form observed on day 112 in 2013, shown in Fig. 2d was somewhat different, in that it was located close to the edge of the main oval, and, as discussed by Badman et al. (this issue), is associated with double sheets of field-aligned current in the outer magnetosphere. Such double sheets of field-aligned current may also be responsible for the wide, apparently bifurcated oval form evident in the image in Fig. 1g. We also observed transient duskside forms, such as that shown in Fig. 2h, which last a few minutes and have been previously observed in the south (Radioti et al., 2009), and further shown by Meredith et al. (2013) to be non-conjugate in the 2009 equinoctial observations. Overall, these forms appear broadly similar to those observed in the south, although the poleward noon

patches of emission are more prevalent than previously observed in the south, and affect the overall statistics of the boundary locations, as discussed in Section 3.2 below.

3.2. Boundary locations

In order to quantify the locations of the auroral boundaries, we have employed an algorithm that fits Gaussians with quadratic backgrounds to latitudinal profiles of intensity integrated over $10°$ of longitude. The boundaries of the auroras are then defined by the locations of the full width at half maximum (FWHM) of the Gaussians. Representative fits and locations thus determined are shown in Fig. 3, where the equatorward boundaries are shown by the yellow crosses and the poleward boundaries by the red crosses, and all the boundaries are shown in a movie (file satnorth-bounds.mov) in the SM. Representative fits to latitudinal profiles are shown in the bottom panels, along with the FWHM locations and associated uncertainty. We have performed this analysis on all the ACS images obtained during both the large ∼60-orbit 2007–2008 program which imaged the southern auroras (we only use ACS images to ensure we are comparing like-with-like) and this 30-orbit 2011–2013 program of observations of the north, and we show the entire set of boundary locations in Fig. 4 using cyan and red points to show the poleward and equatorward locations, respectively. Also shown on the figure by the green and blue solid lines are the mean equatorward and poleward locations,
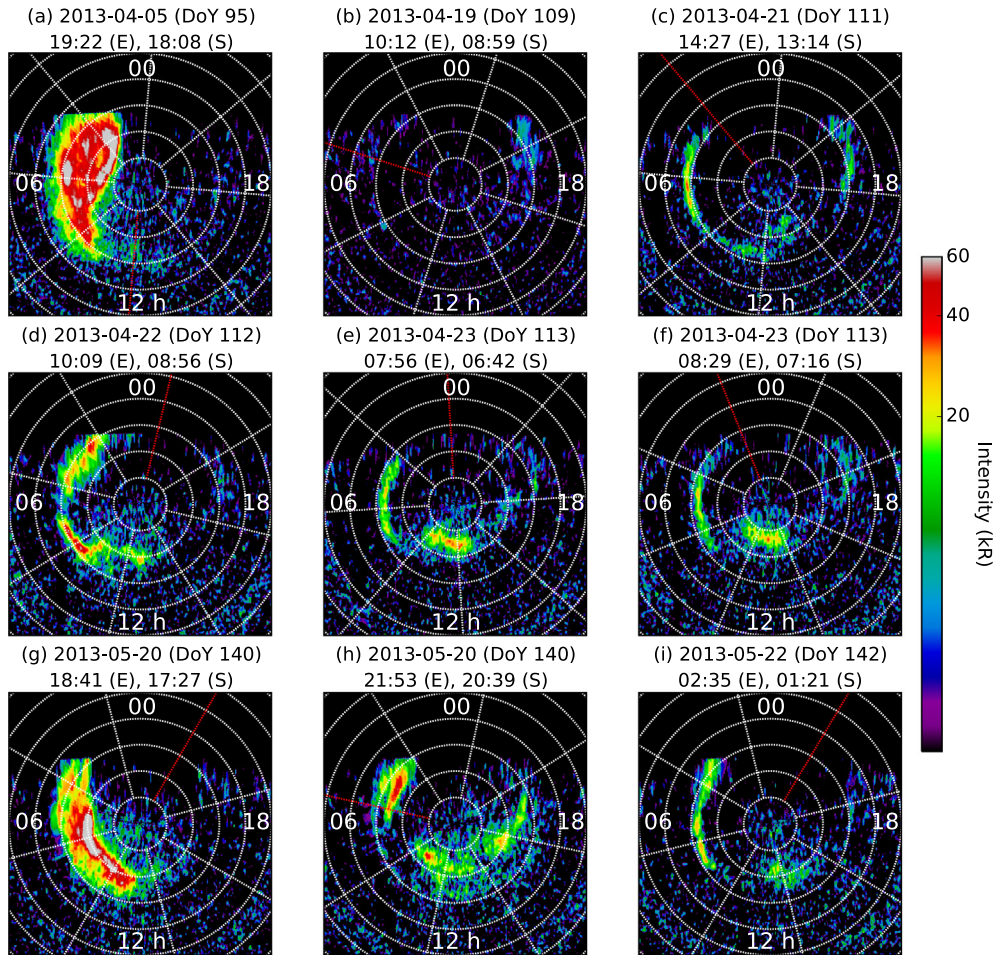
Fig. 2. As for Fig. 1 but for images obtained in 2013.

respectively, determined in 10° azimuth bins (equivalent to 40 min local time (LT)), where azimuth φ increases anti-clockwise as viewed from the north from 0° at noon. The means and standard deviations of the southern boundary locations in each bin are tabulated in Table 1, along with the overall mean and standard deviation. Results for the north are similarly displayed in Table 2. The overall co-latitude distributions are also shown in Fig. 5b and c, where the blue and green histograms represent the equatorial and poleward boundary results, respectively. Considering first the southern boundaries, we note that this represents a significantly expanded sample compared to the previous statistical boundary determinations by Badman et al. (2006), who examined 22 orbits of STIS images of the southern auroras obtained between 1997 and 2004, and whose statistical boundaries are shown for comparison using similarly-coloured dashed lines in Fig. 4a. Accordingly, the variance of our southern boundary determinations is smaller, with overall standard deviations for the south of $\sim1.9°$ and $\sim3.4°$ for the equatorward and poleward boundaries, respectively, compared with Badman et al.'s (2006) values of $\sim2.4°$ and $\sim3.8°$ for the same. These variances give an indication of the changes in latitude of the boundaries owing to magnetospheric dynamics.

As is evident from both Figs. 3a and 5b, the shapes of the latitude distributions of both poleward and equatorward boundaries are skewed toward smaller co-latitudes, with the smaller values generally being located on the dusk side. The overall mean (median) co-latitudes of $\sim17.4°$ ($\sim17.7°$) for the equatorward boundaries, and $\sim13.5°$ ($\sim14.4°$) for the poleward boundaries are

formally consistent with Badman et al.'s (2006) median values of $\sim16.3°$ and $\sim13.9°$, the $1-\sigma$ ranges of which are shown by the horizontal lines in Fig. 5b. Having said this, on the morning side our boundary determinations are consistently modestly equatorward of Badman et al.'s (2006) locations, with average values of $\sim18.0°$ and $\sim15.0°$, i.e. equatorward of Badman et al.'s (2006) values in this region by $\sim1.5°$ and $\sim1.0°$ for the equatorward and poleward boundaries, respectively. In the post-noon sector, our equatorward boundaries, located on average at $\sim16.6°$, are broadly consistent with $\sim0.5°$ with those of Badman et al. (2006), while the poleward values are, at $\sim11.6°$, on average $\sim2.0°$ poleward. Also shown by the coloured dot-dashed lines for comparison are the statistical boundaries of Carbary (2012), determined using Cassini UVIS data obtained over 2007–2009. Although it is important to bear in mind that observations made at different times with instruments may be expected to differ significantly, again our boundaries are broadly consistent within the uncertainties with these boundaries. The notable differences being a consistent $\sim1°$ poleward displacement of the equatorward boundary, and a $\sim2°$ equatorward offset of the poleward boundary in the dusk sector, such that our boundary lies roughly mid-way between the boundaries of Badman et al. (2006) and Carbary (2012).

Turning now to the northern boundaries shown in Fig. 4b, whose latitudinal distribution is shown in Fig. 5c, we again find both distributions are skewed toward smaller co-latitude values, even to the point of exhibiting bimodalities in the distributions which we discuss below. Overall, however, the mean (median) latitude values are $\sim14.6°$ ($\sim15.1°$) $\pm2.3°$ for the equatorward
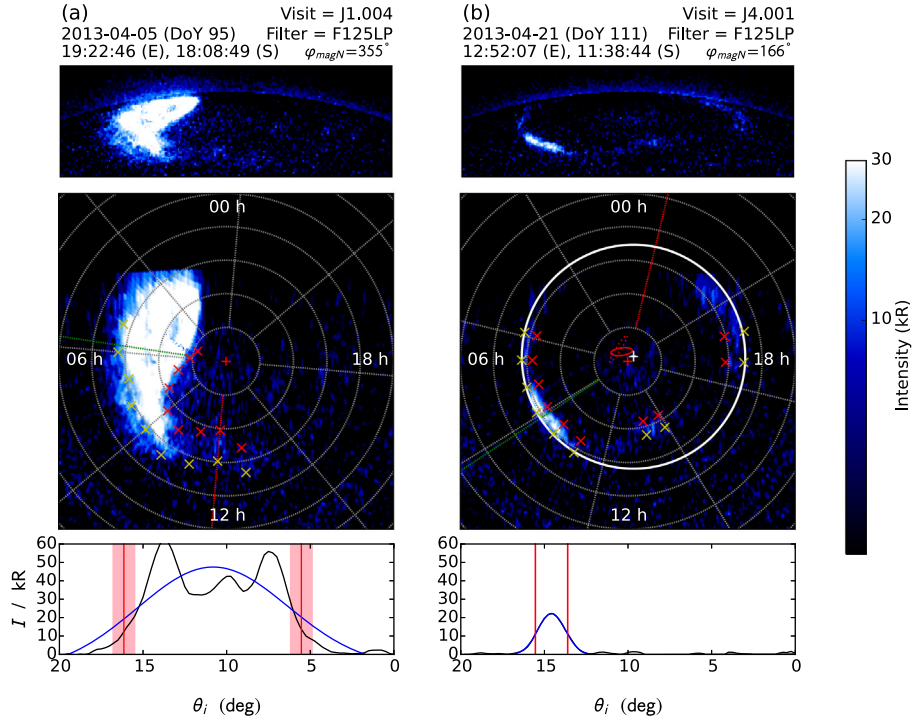
Fig. 3. Figure showing two example images with the computed poleward and equatorward boundaries overplotted with the red and yellow crosses, respectively. The unprojected and projected images are shown, with the latter in the same format as Fig. 1. At the bottom of each panel, representative latitudinal intensity profiles along the meridians highlighted in green in the projections are shown. The Gaussian fits are shown in blue, and the $1 - \sigma$ envelope of the FWHM locations are shown by the vertical red lines and shaded regions. The best fit ellipse for the oval motions observed in this program (solid line) and the 2008 program (dotted line) are shown in red, along with a red cross indicating the spin pole. In panel (b) the best fit circle is shown by the white circle, and its centre is shown by the white cross, with the length of the arms of the cross indicating the uncertainties in each direction as given by the fitting procedure. (For interpretation of the references to colour in this figure legend, the reader is referred to the web version of this article.)
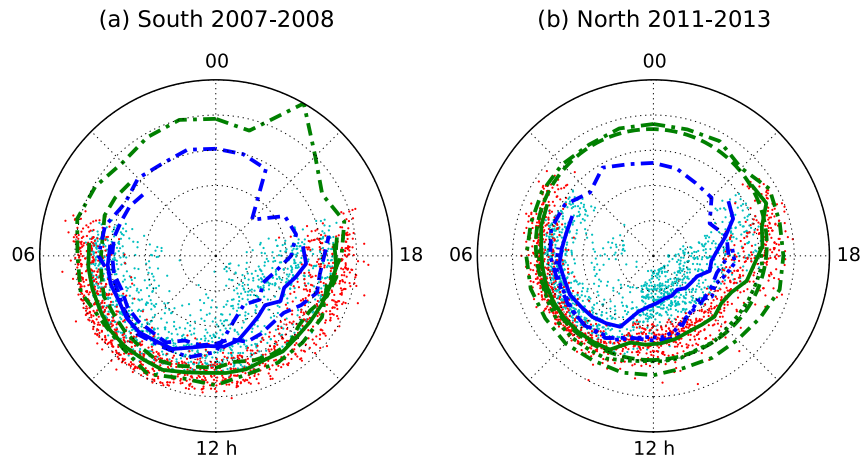

Fig. 4. Figure showing all the boundary points computed, with the poleward locations shown with cyan dots, and the equatorward locations shown in red for (a) the 2007–2008 images of the southern auroras and (b) the 2011–2013 images of the northern. Also shown are binned poleward and equatorward boundaries by blue and green lines, respectively. Our mean boundaries are shown by the solid lines, and in panel (a) those of Badman et al. (2006) are shown by the dashed lines, and those of Carbary (2012) are shown by the dot-dashed lines. In panel (b) our southern boundaries from panel (a) mapped along magnetic field lines using the 'Cassini 5' magnetic field model are shown by the dotted lines, the mean circle fitted to equatorward boundaries of the IR auroras as determined by Badman et al. (2011) are shown by the dashed lines, and the UVIS boundaries determined by Carbary (2012) are shown by the dot-dashed lines. (For interpretation of the references to colour in this figure legend, the reader is referred to the web version of this article.)

boundaries and ∼10.3° (∼11.2°) ±2.3° for the poleward boundaries. It is interesting to compare the flux tubes on which the conjugate mean boundary locations lie. This is illustrated in Fig. 5a, in which the blue and red solid lines indicate the magnetic flux contained within co-latitude θ_i for the north and the south, respectively, using the 'Cassini 5' magnetic field model of Cao et al. (2012), while the vertical coloured dashed lines indicate the mean equatorward

boundary locations, the horizontal dashed lines show the implied contained flux and the coloured shaded areas represent the 1-σ ranges. We use the equatorward boundaries here as they are less affected by sporadic poleward forms, and consequently the latitudinal distribution is narrower, as can be seen in Fig. 5b and c. The fluxes contained within the mean northern and southern equatorward boundaries are ∼46 ± 14 GWb and ∼53 ± 11 GWb, such that

Table 1

Table showing the mean co-latitudes $\langle\theta\rangle$ and associated standard deviations σ in degrees for the southern equatorward and poleward boundaries (substscripts 'eq' and 'pl', respectively), over 10° phase bins centred on phase φ increasing anti-clockwise from zero at midnight.

$\varphi°$ (LT)	$\langle\theta_{eq}\rangle$	σ_{eq}	$\langle\theta_{pl}\rangle$	σ_{pl}
265 (05:40)	18.1	1.7	15.1	2.8
275 (06:20)	18.2	1.5	15.4	2.6
285 (07:00)	18.1	1.6	15.5	2.5
295 (07:40)	18.2	1.6	15.2	2.8
305 (08:20)	18.3	1.4	15.4	2.5
315 (09:00)	18.2	1.6	15.4	2.3
325 (09:40)	18.0	1.6	14.8	2.9
335 (10:20)	17.9	1.3	14.6	2.4
345 (11:00)	17.1	1.7	13.5	2.9
355 (11:40)	16.7	1.6	12.8	3.0
5 (12:20)	16.7	1.7	13.0	2.7
15 (13:00)	16.7	1.5	12.4	3.1
25 (13:40)	16.3	1.5	11.2	3.3
35 (14:20)	16.6	1.7	10.5	4.4
45 (15:00)	16.3	2.0	9.9	4.4
55 (15:40)	16.3	2.1	11.2	4.1
65 (16:20)	16.5	2.3	10.7	3.9
75 (17:00)	16.8	2.4	11.7	3.2
85 (17:40)	17.2	2.2	12.9	3.0
95 (18:20)	16.9	2.2	12.5	3.2
Overall	17.4	1.9	13.5	3.4

the difference between the two is ~7 ± 18 GWb, i.e. consistent with zero. However, all things being equal, the two values of contained flux should be identical, and the degree to which they are not reveals either statistical variance in the results, an inaccuracy in the magnetic field model at ionospheric altitudes, or the effect of some external process on the mean equatorial boundary location, as discussed further below.

We now consider the LT variation of the northern boundaries, shown in Fig. 4b, in which we also show for comparison our southern boundaries mapped along magnetic field lines using the 'Cassini 5' magnetic field model (dotted lines), the mean circle fitted to equatorward boundaries of the IR auroras as determined by Badman et al. (2011) (dashed lines) and the UVIS boundaries

Table 2

As for Table 1 but for the northern auroras.

$\varphi°$ (LT)	$\langle\theta_{eq}\rangle$	σ_{eq}	$\langle\theta_{pl}\rangle$	σ_{pl}
245 (04:20)	16.7	1.1	12.8	2.4
255 (05:00)	16.5	1.3	12.8	3.2
265 (05:40)	16.0	1.3	13.0	2.8
275 (06:20)	15.8	1.1	13.4	2.1
285 (07:00)	15.8	1.2	13.1	2.5
295 (07:40)	15.6	1.1	13.1	1.8
305 (08:20)	15.4	1.0	12.6	2.3
315 (09:00)	15.2	1.1	12.3	2.2
325 (09:40)	14.9	1.1	11.7	2.4
335 (10:20)	14.7	1.7	11.1	2.8
345 (11:00)	12.8	1.7	8.2	2.9
355 (11:40)	12.7	1.7	7.2	2.7
5 (12:20)	12.5	1.6	6.7	2.5
15 (13:00)	12.2	2.0	6.2	2.2
25 (13:40)	11.9	1.5	6.3	2.2
35 (14:20)	12.0	1.2	5.9	2.2
45 (15:00)	12.2	1.7	6.5	2.3
55 (15:40)	11.8	1.5	6.6	2.1
65 (16:20)	12.2	2.0	6.9	2.2
75 (17:00)	13.7	2.5	8.3	3.3
85 (17:40)	14.3	2.4	8.3	3.7
95 (18:20)	15.5	2.4	9.1	3.7
105 (19:00)	15.9	2.3	10.6	3.2
115 (19:40)	17.7	1.3	12.5	2.2
125 (20:20)	17.2	1.4	13.1	1.5
Overall	14.6	2.3	10.3	3.8

determined by Carbary (2012) (dot-dashed lines). It is first evident that the nature of the boundaries changes somewhat abruptly at 10–11 h LT. At earlier local times the equatorward boundary locations, located on average at ~15.7°, are consistent with both the mapped southern boundaries and the mean circle representing the equatorward edge of the IR emissions. It is, however, ~2° poleward of the equatorward boundary of Carbary (2012), which remains ~2–3° equatorward of the IR and mapped southern boundaries over all LTs at which they are all measured. Staying in the post-dawn sector, the poleward boundary, which is located on average at ~12.6° in this region, is also closely consistent with the mapped southern boundary near 6 h LT, but diverts ~2° poleward of the mapped southern and Carbary (2012) boundaries toward 10 h. At later local times, both equatorward and poleward boundaries jump abruptly poleward, such that the average values over this region are ~13.6° and ~8.2°. In the post-noon sector the equatorward boundaries are ~3° poleward of both the mapped southern boundary and the mean IR circle, which are consistent with each other, and up to ~5° poleward of the Carbary (2012) equatorward boundary, but nearer to ~18 h our boundary again moves equatorward toward values consistent with the latter boundaries later than ~18°. The poleward boundary, on the other hand, remains ~3–4° poleward of the mapped southern boundary,
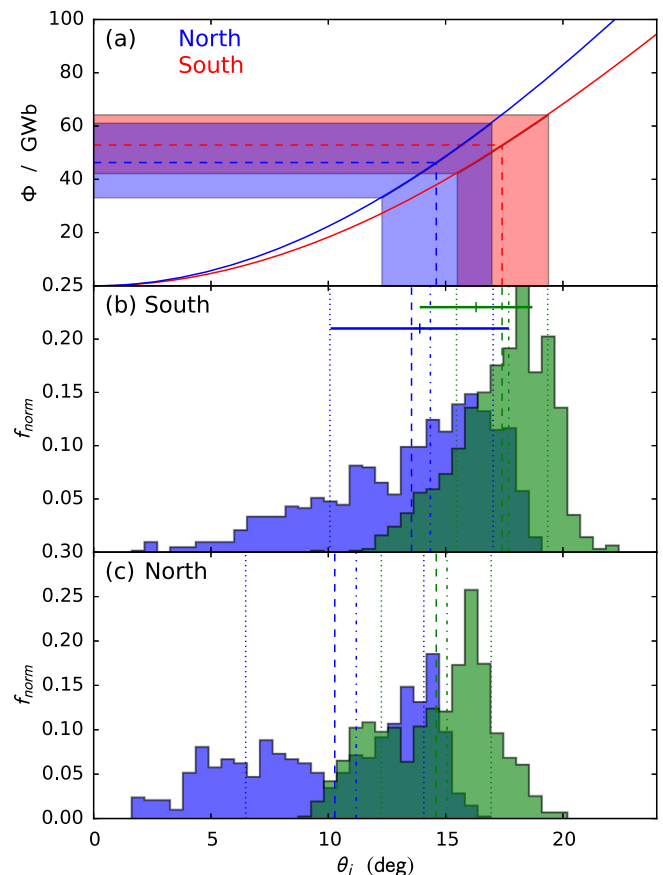

Fig. 5. Figure showing normalised histograms of the equatorward (green) and poleward (blue) boundary co-latitudes for (panel b) the south and (c) the north. The distribution means (medians) are indicated by the dashed (dot-dashed) lines, and the $1 - \sigma$ ranges about the means are shown by the dotted lines. In panel (b) the horizontal lines indicate the means and $1 - \sigma$ range of the Badman et al. (2006) boundaries. In panel (a) we show the magnetic flux Φ in GWb contained within co-latitude θ_i for the south (red solid line) and the north (blue solid line). The similarly-coloured vertical dashed lines with shaded areas show the mean and $1 - \sigma$ ranges of the equatorward boundaries, and the horizontal regions indicate the corresponding magnetic fluxes. (For interpretation of the references to colour in this figure legend, the reader is referred to the web version of this article.)

which remains consistent with the Carbary (2012) poleward boundary over the whole dusk-side region where southern boundaries are available. The abrupt change in behaviour at 10–11 h between generally equatorward values at earlier local times and more poleward values thereafter, gives rise to the bimodality apparent in the latitude distributions plotted in Fig. 5c. We discuss an interpretation of these boundary locations in Section 4, and turn now to circle fits derived from these boundary locations.

Following Nichols et al. (2008), in those cases where the auroras exhibit the typical 'quiet time' morphology and the locations of the boundaries are constrained on both the dawn and dusk sides, as shown by the representative example in Fig. 3b, we have fitted circles to the equatorward boundaries. This technique was employed by Nichols et al. (2008) in order to discover and examine the near-planetary period oscillation of the southern auroral oval. An example of such a fitted circle to a northern aurora image is shown in Fig. 3b, and a movie (file circsnorth.mov) showing all the fitted circles is available in the SM. Owing to the poleward distortion of the auroral boundaries in the noon and afternoon sectors discussed above, we exclude points in the phase range $160° < \varphi < 250°$ for purposes of circle fitting. These fitted circles are useful as they yield an estimate for the co-latitudinal radius of the oval that is independent of the oval oscillation phase and any poleward distortions in the post-noon sector, as well as providing the location of the oval centre.

First, in order to examine further the conjugate flux mapping of the mean latitudes of the equatorward boundaries, we show in Fig. 6b the distributions of circle co-latitude radii, with results for the south shown in red and those for the north in blue. Also shown in Fig. 6a is the associated enclosed flux, in the manner of Fig. 5a above. It is first apparent that the distributions are narrower than in Fig. 5, owing to both the selection of only quiet time images and the existence of only a single best-fit radius value for each image. The mean radii of ~17.8° (south) and ~16.3° (north) correspond to encircled magnetic fluxes of ~55 ± 8 GWb and ~57 ± 16 GWb, such that the difference here is ~2 ± 18 GWb, i.e.

Fig. 6. As for Fig. 5 except for the fitted circle radii r_i, with results for the south shown in red, and form the north shown in blue. (For interpretation of the references to colour in this figure legend, the reader is referred to the web version of this article.)

consistent with zero, and significantly smaller than the result given by the individual latitude values. This implies that the difference in the previous case is likely due to increased prevalence of afternoon sector poleward forms observed in the northern data set, that do not affect the fitted circle results here.

3.3. Planetary-period oscillations

Despite the high degree of axisymmetry of Saturn's internal magnetic field, oscillations are observed ubiquitously throughout the magnetosphere in many phenomena associated with the planet's magnetic field (see e.g. the review by Carbary and Mitchell (2013) and references therein). These planetary period oscillations (PPOs) and their magnetic signatures within the Saturnian magnetosphere have been extensively studied by Andrews et al. (2010, 2012) and Provan et al. (2011, 2013). We now consider the modulation of the auroral location and intensity with magnetospheric PPO phase as determined from the magnetometer observations. Before we examine the HST results, however, it is worth considering the PPO context for each observing intervals. Kurth et al. (2008) showed that there are two distinct PPO periods, and Gurnett et al. (2009) demonstrated that one period emanates from the northern hemisphere and one from the southern. Andrews et al. (2012) demonstrated that within the northern (southern) polar cap region only purely northern (southern) oscillations can be detected. However, Provan et al. (2011) demonstrated that within the closed equatorial 'core' region of Saturns magnetosphere (taken to correspond to dipole $L < 12 R_s$) both the oscillations are present, and that their amplitudes vary over time. Moreover, Provan et al. (2013) showed that since the beginning of 2011 a number of sharp changes in the amplitude of the two oscillations. Near southern solstice, the amplitude of the southern PPO signal dominated the northern by a factor of ~2.5, while from post-equinox in 2009 up to February 2011 (dubbed interval E1 by Provan et al. (2013)) the amplitudes of the two signals became comparable. Thereafter, the dominance has abruptly flipped a number of times between hemispheres. From February–August 2011 (interval E2) the southern signal resumed (weaker) dominance, while from August 2011 to April 2012 (interval E3) the northern signal strongly dominated the southern, which was essentially non-existent during this interval. During April 2012 the northern amplitude then also abruptly decreased to zero, and both signals gradually returned (interval E4), with modest northern dominance until December 2012, when both signals became comparable (interval F1). During February 2013 the southern signal then resumed weak dominance over the northern, until July 2013. Thus, during all observing intervals with the exception of that during 2012, the southern signal either strongly or weakly dominated the northern in the magnetosphere. The 2012 observing program lay toward the very end of interval E3, i.e. strongly dominated by the northern signal, and only a few days following the end of the HST observations the PPO signals abruptly vanished. This interesting interval is presently the subject of ongoing investigation and here we simply note its near-coincidence with the HST observations. It should be noted, however, that the southern PPO phases during interval E3 have no physical grounding, in that they do not organise the magnetic field data during this period, and are computed from interpolation between intervals E2 and F1.

As shown by Andrews et al. (2010), the rotating magnetic perturbations are associated with a primary system of electric currents which flow along the magnetic field into one ionosphere on one side, then across the polar region as ionospheric Pedersen currents and back out along field lines on the other side. The currents then close through the equatorial plane and, possibly, partially through a secondary, opposite-polarity current system flowing through the conjugate ionosphere (Southwood and Kivelson, 2007).
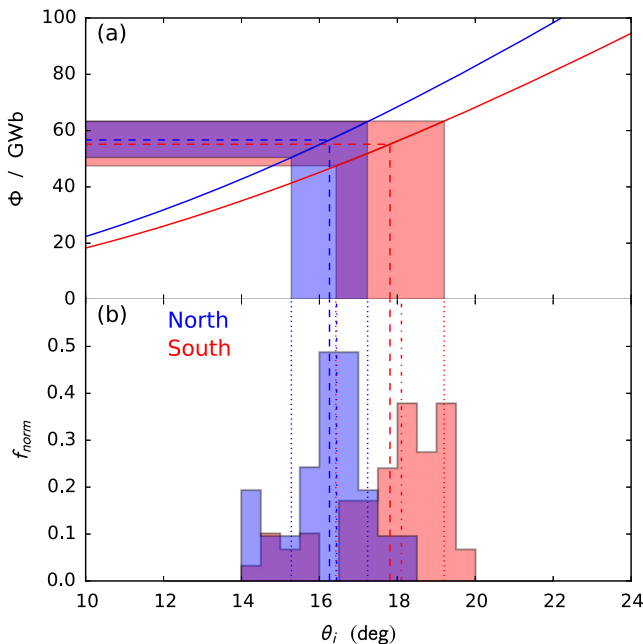
The current systems have recently been shown to be of the sense such that they transfer angular momentum from the ionosphere to the magnetosphere (Hunt et al., 2014), and the upward components are coincident with the locations of the auroras as given by the Carbary (2012) boundaries. The PPOs are each characterised by phase $\phi_{mag N,S}(t)$, which cycles through 360° in period $\tau_{N,S}$, where the subscript N or S denotes the hemisphere with which the phase is associated, and phase $\phi_{mag N,S}$ indicates the anti-clockwise (as viewed from the north) azimuthal angle from noon of the quasi-uniform equatorial perturbation field. A PPO 'longitude' system can then be defined, such that 'longitude' $\Psi_{mag N,S}(\varphi,t) = \phi_{mag N,S}(t) - \varphi$. As discussed above, Nichols et al. (2010a) presented evidence that the UV auroras exhibit patterns fixed in both ($\phi_{mag S}$, LT) and $\Psi_{mag S}$, i.e. a time-varying, periodic pulsing in intensity superposed on a weaker rotational modulation in intensity and in location. Before examining how the intensity varies with PPO phase, we first consider the location of the northern auroras as observed in these HST images.

The oscillation of the location of the southern auroras was discovered by Nichols et al. (2008), and the modulation of the northern auroras by PPO phase was studied by Nichols et al. (2010b), who examined equinoctial images in which highly oblique views of the both ovals were obtained. They presented some evidence that the northern oval oscillates in at least the dawn–dusk direction with the northern SKR phase $\varphi_{SKR N}$ (defined such that the dawnside northern SKR emission peaks in intensity at $\varphi_{SKR N} = 0°$, and is related to the magnetic PPO phase by $\varphi_{SKR N} \simeq \phi_{mag N}$), and, although formally significant, the correlation coefficient r between the dawn–dusk location and $\sin(\varphi_{SKR N})$ was a somewhat low ~0.47. Comparison of the location of the respective southern and northern auroral ovals with PPO phase led Provan et al. (2009) and Nichols et al. (2010b) to conclude that the offsets of the centres of both ovals are consistent with a displacement in the direction of the effective dipole axes of the perturbation fields, as appropriate for each hemisphere (Provan et al., 2009; Nichols et al., 2010b), i.e. toward $\Psi_{mag N} = 0°$ and $\Psi_{mag S} = 180°$ for the north and south, respectively. Thus, considering simply a circular motion, we have maximum duskward displacement of the ovals at $\phi_{mag S} = 270°$ and $\phi_{mag N} = 90°$ for the southern and northern ovals, respectively. However, recent work examining the PPO modulation of the co-latitudes of the southern field-aligned current signatures observed in the Cassini magnetometer data (Hunt et al., 2014) indicates that the upward field-aligned currents associated with the southern auroral emission are in fact displaced toward the direction of $\Psi_{mag S} = 270°$, or 90° behind the effective dipole displacement in the south, such that we may expect e.g. maximum duskward displacement of the southern oval at $\phi_{mag S} = 0°$. For the north, a similar effect would imply a displacement toward $\Psi_{mag N} = 90°$, i.e. with maximum duskward offset at $\phi_{mag N} = 180°$. Caveats to this result are that they are based on data obtained over a narrow LT range, between ~0–4 h, and that it is presently unknown if such an effect is actually also present in the north. However, in light of this apparent disconnect between different sets of previous observations, we now discuss the oscillation as observed using the more complete views of the northern images presented here.

Following Nichols et al. (2008), we have plotted the coordinates of the centres of the obtained circle fits to the northern auroras versus $\phi_{mag N}$. The coordinate system for the circle centres is oriented such that x is positive toward the Sun and y is positive toward dusk. The coordinates of the oval centre versus $\phi_{mag N}$ are then shown by the crosses in Fig. 7, along with best fit sinusoidal functions of the form $f(\phi_{mag N}) = \alpha \sin(\phi_{mag N} - \phi_0) + \beta$, shown by the solid lines. The associated dark grey shaded areas indicate the combined $1 - \sigma$ range arising from the uncertainty in amplitude and vertical offset of the best fit function parameters,
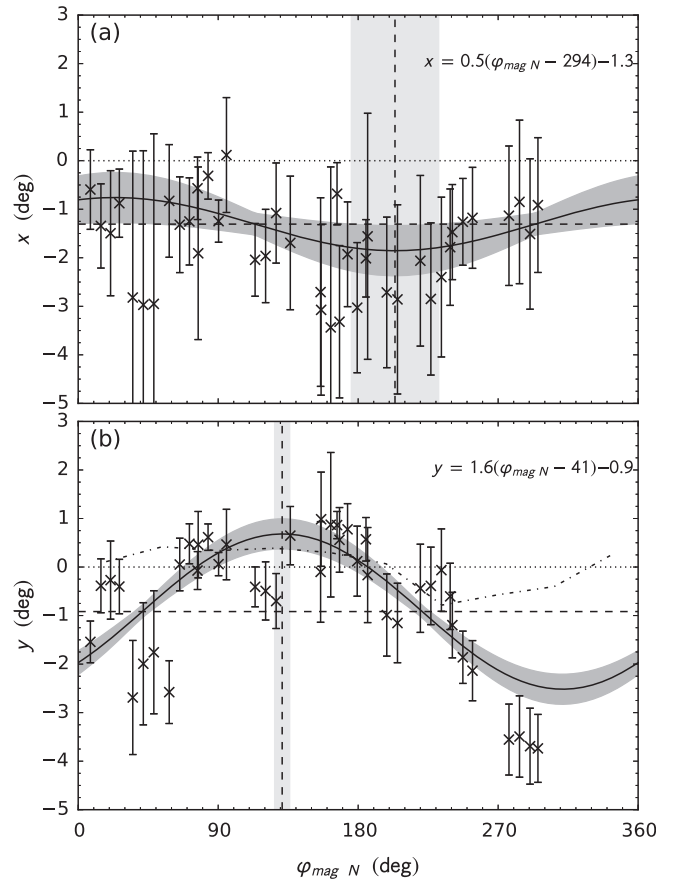

Fig. 7. Figure showing the locations in degrees of co-latitude of the circles fitted to the northern auroras in the (a) x (positive sunward) and (b) y (positive duskward) directions versus PPO phase for northern PPO system $\phi_{mag N}$. The error bars indicate the uncertainty in the location of the circle fit. The best fit sinusoidal functions are shown by the solid lines, whose equations are shown in the top right of each panel. The associated dark grey shaded areas indicate the combined $1 - \sigma$ range arising from the uncertainty in the amplitude and vertical offset of the best fit function parameters. The dashed vertical line indicates the location of maximum duskward displacement, while the associated vertical light grey region indicate the $1 - \sigma$ uncertainty in phase offset φ_0. In panel (b) the binned dawn–dusk location of the northern oval as determined by Nichols et al. (2010b) is shown by the dot-dashed line.

while the vertical light grey region indicates the $1 - \sigma$ uncertainty in phase offset ϕ_0. The binned dawn–dusk location of the northern oval as determined by Nichols et al. (2010b) is shown by the dot-dashed line in Fig. 7b. It is apparent that the oscillation, while present in both components, is only well constrained in the dawn–dusk, or y, direction, owing to the fact that the midnight sector of the auroral region is still not visible on the limb of the planet, and is thus not present in the projected images used in the analysis. The oscillation amplitudes for the noon–midnight and dawn–dusk directions are $\sim 0.5 \pm 0.3°$, and $\sim 1.6 \pm 0.2°$, respectively. Thus, while both oscillations are significant in amplitude, the dawn–dusk component oscillation is clearly most well constrained, with a best-fit sinusoidal amplitude that is a factor of ~3 larger than observed in the 2009 equinoctial images, and larger than most observations of southern oscillation components. The phasing of the fit is such that maximum duskward displacement occurs at $\phi_{mag N} \simeq 131° \pm 5°$, i.e. not formally consistent with a circular displacement caused by either paradigm discussed above, but is nearly midway between the two.

Together, the oscillations in the two components form a Lissajous ellipse as discussed by Nichols et al. (2008), and the phase

of the maximum duskward displacement is then a function of the ellipse geometry. We plot the resulting ellipse for the northern PPO phase by the solid red line in Fig. 3b, along with that obtained from the 2008 southern data shown by the dotted ellipse for comparison. The northern aurora ellipse is, like the southern, highly eccentric, with eccentricity $\epsilon \simeq 0.95$ and semi-major axis $a = \simeq 1.6 \pm 0.2°$, the latter being slightly less than that observed in 2008 but reasonably consistent with observations of the oscillations in the field-aligned currents (Bunce et al., 2014). Thus, the overall amplitude of the oscillation is consistent with observations of the south, except that the low amplitude in the x-direction results in an ellipse oriented more toward the dawn–dusk direction than observed for the south. However, bearing in mind the lack of constraint in the x direction, it is unclear from these results whether this is real.

We now turn to the variation in the aurora intensity with PPO phase. The rotating pattern of field-aligned currents in each ionosphere owing to the above-described magnetic perturbation current systems, fixed in $\Psi_{mag\,N,S}$, is shown in Fig. 8. The pattern is shown as viewed from the north for both ionospheres, i.e. through the planet in the case of the south, such that green circles with dots represent upward current for the north and downward current for the south, and vice versa for green circles with crosses. The pattern is the same for both hemispheres and primary and secondary (i.e. inter-hemispheric) current systems, although we note that the auroral brightness, which is maximum for upward-directed field-aligned current associated with downward-precipitating electrons, is opposite for the two hemispheres. Thus, the auroral brightness is expected to peak at $90°$ in the north and $270°$ in the south for both primary and secondary current systems, as highlighted by the red labels in Fig. 8. In addition to this pattern fixed in $\Psi_{mag\,N,S}$ there is a superposed variation fixed in ($\phi_{mag\,N,S}$, LT), such that the field-aligned currents are most intense when $\phi_{mag\,S} = 180°$ and $\phi_{mag\,N} = 0°$, resulting in the pulsing of the total auroral and SKR emitted power, originating from emissions on the dawnside

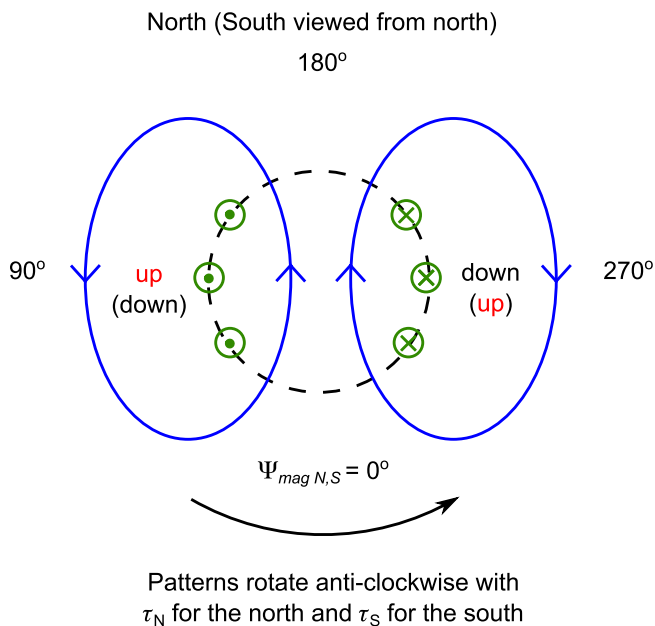**North (South viewed from north)**

Fig. 8. Schematic showing the form of the PPO currents as viewed from the north in the rotating frame of each current system. The pattern is the same for both hemispheres and both primary and secondary (inter-hemispheric) current systems. The sense of the field-aligned currents is shown by the green symbols and the associated perturbation fields are shown by the blue lines. The sense of the currents relative to the ionospheres are shown by the text (bracketed for the south), and the upward currents are highlighted in red. (For interpretation of the references to colour in this figure legend, the reader is referred to the web version of this article.)

(Kurth et al., 2007; Nichols et al., 2010a; Lamy et al., 2009). As discussed above, Nichols et al. (2010a) showed that the UV auroras exhibit intensity patterns fixed in both ($\phi_{mag\,S}$, LT) and $\Psi_{mag\,S}$, Carbary (2013) has also shown using Cassini UVIS data that the southern auroras exhibit a strong unimodal intensity variation with SKR phase, with a peak near $\Psi_{SKR\,S} \simeq 200°$, whereas the northern auroras are, by comparison, remarkably constant with $\Psi_{mag\,N}$. In addition, Badman et al. (2012b) showed that in each hemisphere the IR auroras exhibit rotational modulation at the PPO phase consistent with the above picture, including weak intensity modulation at the phase of the opposite hemisphere, providing evidence that part of the southern current system closes in the northern hemisphere.

Considering now the observed variation in intensity observed in the northern auroras, we show, following Nichols et al. (2010a), the mean maximum auroral intensity (corrected simply for limb-brightening by multiplication with the cosine of the viewing angle (Grodent et al., 2005); note, however, that the following results do not sensitively depend on this correction) obtained along meridional cuts between $10°$ and $20°$ co-latitude averaged over 0.5 h LT bins for non-storm-time images, thus considering the variation of the quiet time main oval only. The storm-time images discounted in this analysis executed on days 97 and 99 in 2011, and 95 and 140 in 2013, each representing 1 orbit except day 140 with 3. The maximum intensity is employed since it provides a simple representation of the field-aligned current density. Note that, as shown in Figs. 1 and 2, we clip the images a few degrees away from the limb to avoid the stretched, very limb-brightened region where the projected intensities become inaccurate. The intensities for each year and the program as a whole are shown as a function of LT-PPO phase space in Figs. 9 and 10 for the northern and southern PPO phases, respectively. Also shown at the top and right of each panel are sums along the respective axes of the figure, and contours of constant $\Psi_{mag\,N,S}$ are shown by dashed red lines. It is first apparent that, as discussed above, the auroras are typically brighter on the dawn side than at dusk, and that they exhibit a number of peaks in intensity on the dawn side. Considering first the results using the northern PPO phase shown in Fig. 9, the 2011 and 2012 data in Fig. 9a and b exhibit enhanced brightness near to $\phi_{mag\,N} = 0°$, i.e. near $\Psi_{mag\,N} = 90°$, consistent with the discussion above. In 2013, there were images obtained near to $\phi_{mag\,N} = 0°$, but they executed on day 95, such that the emissions were dominated by the solar wind-induced storm and were therefore not used in the present analysis. It is therefore unknown whether a similar peak occurs at dawn near $\phi_{mag\,N} = 0°$ for 2013. There is a peak at dawn in Fig. 9c between $\phi_{mag\,N} \simeq 90$ and $180°$, which appears to remain fixed between $\Psi_{mag\,N} = 180$ and $270°$, but a peak at this phase is not obviously connected with the northern PPO currents. Overall, on the dusk side there is a suggestion of a possible broad, shallow peak in intensity between $\phi_{mag\,N} \simeq -90$ and $0°$ in Fig. 9d, but again this is not obviously associated with the northern PPO currents. Taken as a whole, there is some evidence of modulation near $\phi_{mag\,N} = 0°$ at dawn, consistent with the northern PPO currents, but there clearly exists some other process(es) able to excite emissions at other PPO phases.

Given the dominance of the southern PPO signal during the 2011 and 2013 observation intervals, it is therefore worth considering the modulation at the southern PPO phase, shown in Fig. 10 in the same format as for the northern PPO phases. However, during 2011 and 2013, the results for which are shown in Fig. 9a and c, respectively, there were no quiet-time images obtained at $\phi_{mag\,S} = 0°$, and note also that, although for completeness we have plotted in Fig. 9b the 2012 intensities versus southern PPO phase as given by Provan et al. (2013), recall that these phases are obtained by interpolation over the E3 interval, such that there is no
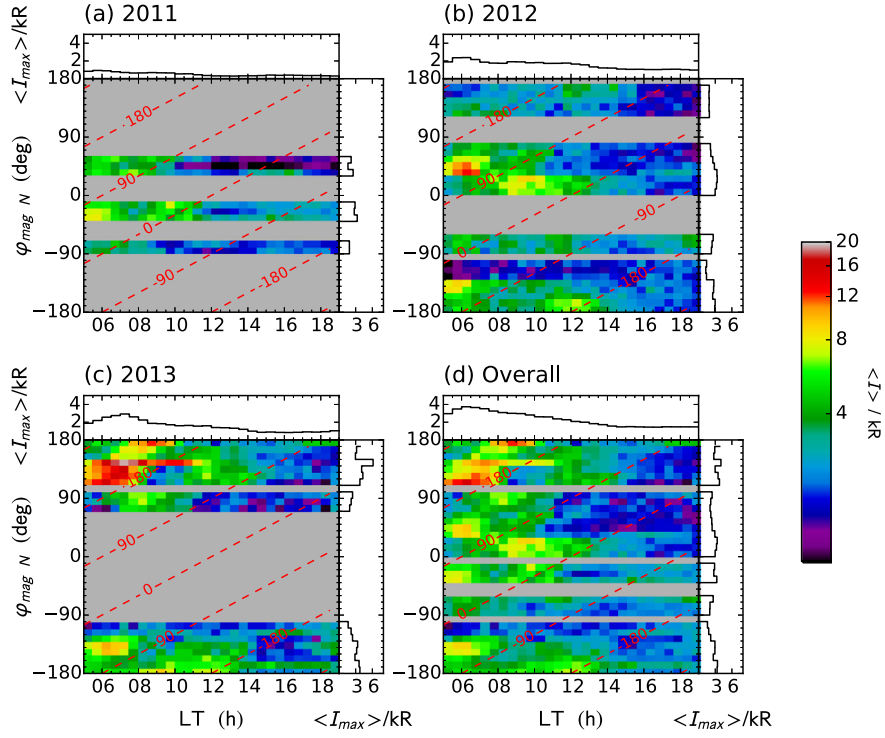
Fig. 9. Figure showing the maximum intensities I_{max} in kR determined as discussed in the text for the northern auroras, in LT-northern PPO phase space for (a) 2011, (b) 2012, (c) 2013, and (d) overall. Lines of constant $\Psi_{mag\,N}$ are shown by the red dashed lines, and data gaps are shown in grey. Means along each axis are also shown by the sub-panels to the top and right of each main panel. (For interpretation of the references to colour in this figure legend, the reader is referred to the web version of this article.)
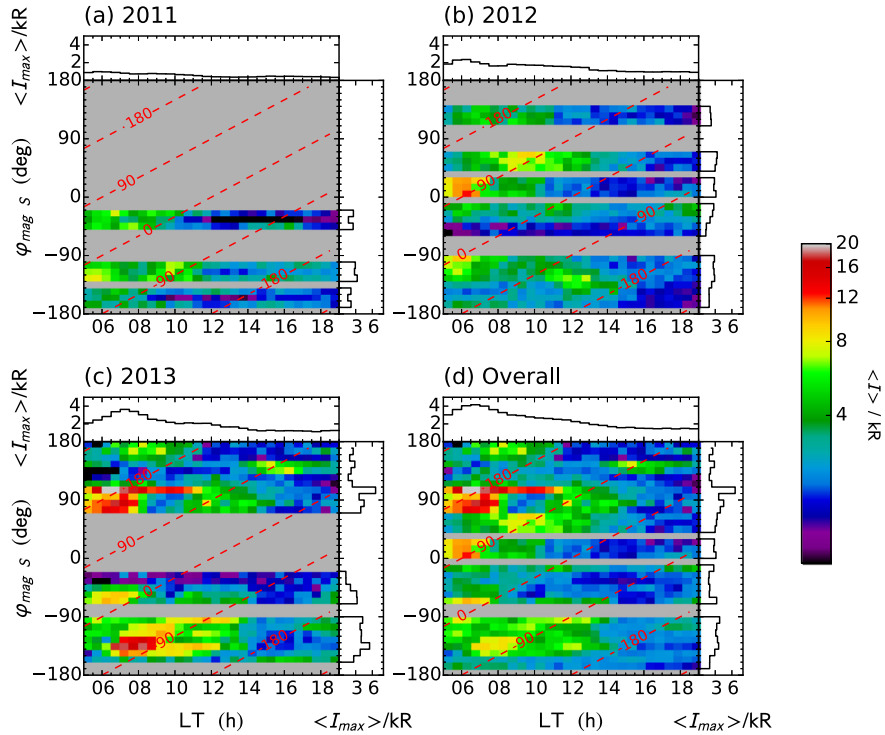

Fig. 10. As for Fig. 9 but for the southern PPO phase.

expectation that they organised the auroral currents during these observations. For 2011, although there is emission on the dawnside in the images obtained close to $\phi_{mag\,S} = 0°$, there is not enough surrounding data to conclude whether this is part of an enhancement above background levels. The peak between $\phi_{mag\,S} \simeq 180$ and $270°$

is just that which occurs at $\phi_{mag\,N} = 0°$, as is likely also the case for the enhancement observed in the 2012 images around $\phi_{mag\,S} = 0°$. The principal enhancements observed in 2013 occur near $\phi_{mag\,S} = 90°$ and between $\phi_{mag\,S} = 180°$ and $270°$, and are again not obviously explained by the southern PPO currents, such that

their origin likely lies elsewhere, perhaps modulated by, e.g. smaller-scale solar wind density variations than those which drive the large storms. Considering the overall results for the southern PPO phase shown in Fig. 10d, it is interesting to note the emission which appears apparently fixed around $\Psi_{mag\,S} = 90°$, comprised of data obtained during all 3 years and which could in principle be consistent with the secondary, inter-hemispheric currents associated with the southern PPO, but given the caveats about the southern PPO results discussed above, we are cautious about ascribing too much physical significance to this observation.

In order to further examine whether there are emissions which are fixed in magnetic 'longitude' $\Psi_{mag\,N,S}$ we have co-added the quiet-time projected images, each rotated such that the direction of $\Psi_{mag\,N,S} = 0°$ is oriented toward the bottom of the figure, thus building up a statistical picture of the emissions in frames which rotate with the two PPO current systems, in a similar manner to that done previously by Carbary (2013). In order to put our analyses of the northern data in context, therefore, we first show in Fig. 11 the co-added images for the 2007–2008 southern auroras, using the southern PPO phase (left-hand column) and the northern PPO phase (right-hand column). Considering first the modulation with the southern PPO phase, it is first apparent that for both the 2007 and 2008 data shown in Fig. 11a and c, enhancements in intensity occur near $\Psi_{mag\,S} = 270°$, i.e. consistent with the expectation on the basis of the southern PPO currents as shown in Fig. 8. However, only very weak, poleward enhancements are present at $\Psi_{mag\,N} = 270°$ for the northern phase results shown in

Fig. 11b and d, and the brighter enhancements at $\Psi_{mag\,N} = 90°$ are opposite to the expectation for secondary northern hemisphere currents such that there is little evidence of any modulation owing to secondary inter-hemispheric currents associated with the northern PPO current system. It is, however, interesting to note that the oval displacement giving rise to the oscillation of the location of the oval with southern PPO phase, as discussed by Nichols et al. (2008), is evident in these images, with the equatorward boundary of the co-added emission lying ~2° poleward in the $\Psi_{mag\,S} = 0–90°$ (i.e. bottom left) sector than the diametrically opposite longitudes, such that the overall displacement is toward $\Psi_{mag\,S} \simeq 225°$, i.e. roughly midway between the effective dipole tilt and field-aligned current displacement paradigms discussed above.

Considering now the northern auroras, we show in Fig. 12 the co-added images in a similar format to Fig. 11. It is worth recalling that, as well the increasing sub-Earth latitude, the number of quiet-time orbits which are employed in this analysis during each year increased from 3 in 2011, through 10 in 2012 to 11 in 2013, such that the noise in the summed images decreases accordingly. Employing the southern PPO phase yields (data gap notwithstanding) a broad enhancement in intensity between $\Psi_{mag\,S} \simeq 0°$ and 90° for 2011 in Fig. 12a, a peak in intensity near $\Psi_{mag\,S} = 90°$ for 2012
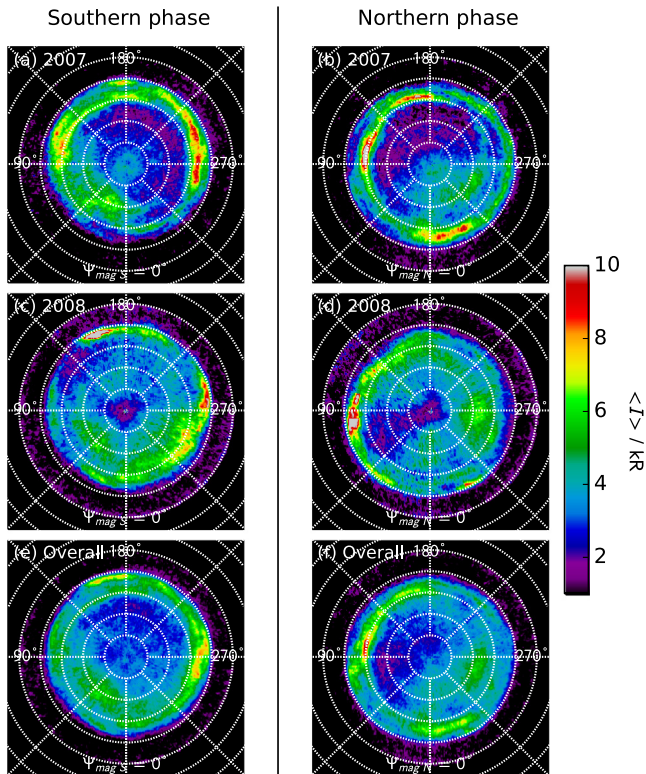
Northern auroras 2011-2013

Fig. 11. Figure showing co-added images (i.e. of the mean intensity per projected pixel) of the southern auroras as observed in 2007–2008, in which each image has been rotated such that $\Psi_{mag\,N,S} = 0°$ is oriented toward the bottom of the figure. The results for the southern PPO phase are shown in the left column and the results for the northern PPO phase are in the right column. The rows show the 2007, 2008 and overall results, respectively. In each panel a $5° \times 45°$ latitude–longitude grid is overlaid by the grey dotted lines.
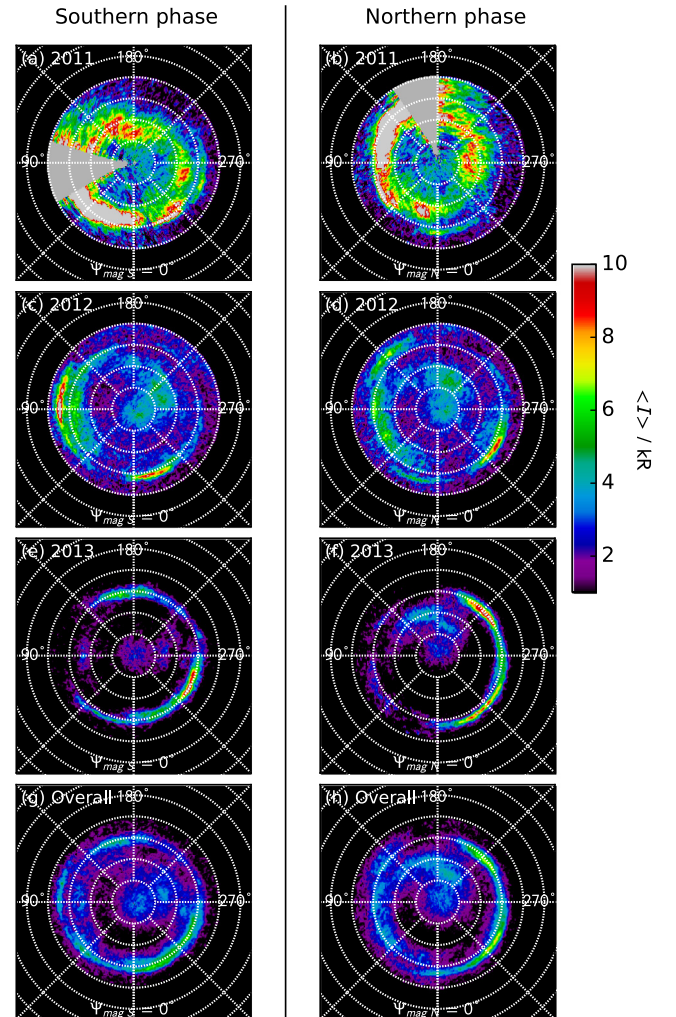
Fig. 12. As for Fig. 11 but for the northern images. A data gap in the 2011 images in the top row is shown in grey.
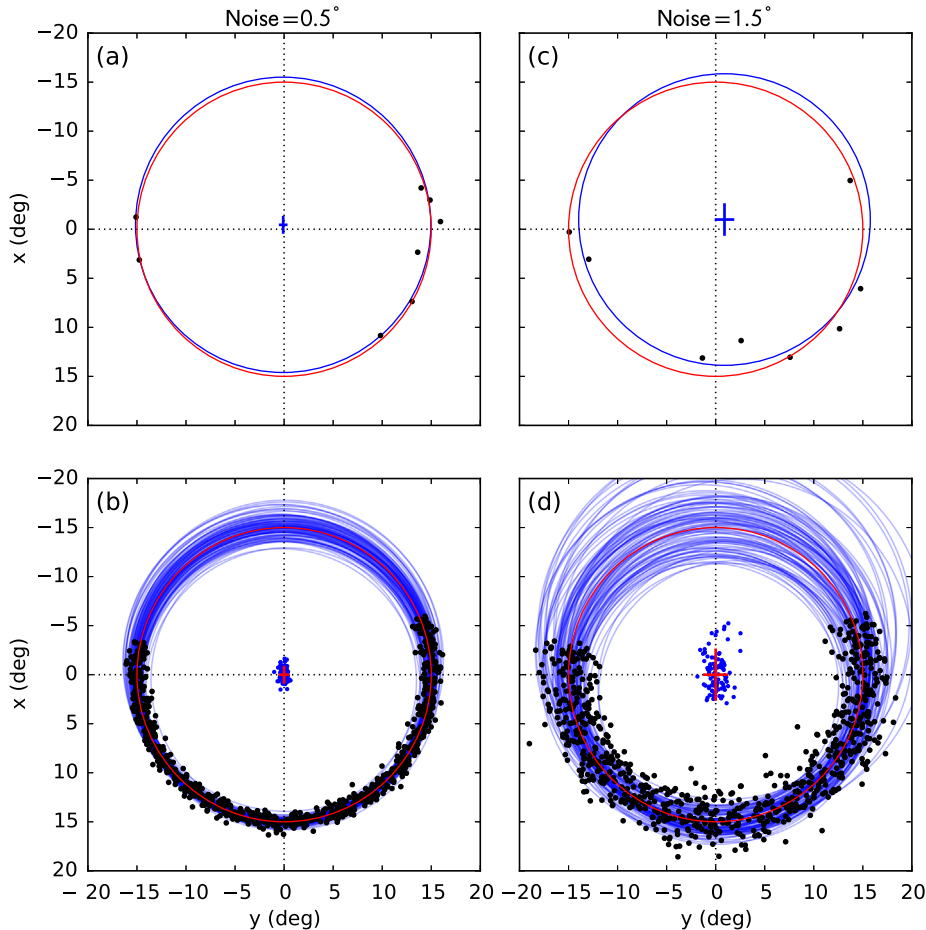
Fig. 13. Circle fits (blue circles) to simulated data (black points) with (left) ∼0.5° and (right) ∼1.5° radial noise about a 15° circle centred on the origin (red circle). In panels (a) and (c) the centre of the fitted circle is shown by the blue cross, with the length of the arms of the cross indicating the uncertainties in each direction. In panels (b) and (d) the centre of each fit is shown by a point, while the red crosses centred on the origin indicate the mean uncertainty values obtained in the fits. (For interpretation of the references to colour in this figure legend, the reader is referred to the web version of this article.)

in Fig. 12c, but no obvious enhancement at $\Psi_{mag\,S} = 90°$ for 2013 in Fig. 12e. Using the northern PPO phase, there exists for 2011 a broad region of bright emission over the interval between $\Psi_{mag\,N} \simeq 0°$ and 180° for 2011 in Fig. 12b, modest emission over the same longitude range for 2012 in Fig. 12d, and again no bright emission in this sector for 2013 in Fig. 12f. On the other hand, enhancements near to $\Psi_{mag\,N} \simeq 270°$ in Fig. 12d and h are opposite to the expectation for the primary current system discussed above. Overall, then, there is some modest evidence for intensity modulation by the northern PPO current system for 2011 and 2012, none for 2013, and again some apparent evidence for modulation by inter-hemispheric secondary currents originating from the southern PPO currents, although we recall the caveats for the southern PPO phases discussed above. Finally, although the northern results are noisier than for the southern, it is worth noting that the oval displacements implied by the oscillations considered above are evident in the overall co-added image in Fig. 12h, i.e. where the oval is reasonably sharply defined on the right hand side, it is displaced ∼2° more equatorward in the $\Psi_{mag\,N} \simeq 0°$ to post-270° (i.e. bottom right) sector than in the $\Psi_{mag\,N} \simeq 180°$ to 270° (i.e. top right) region.

4. Summary and discussion

In this paper we have discussed the statistics of the northern auroras of Saturn as observed during a program of HST/ACS

observations over the post-equinox interval 2011–2013, and compared the overall behaviour with that exhibited by previous HST/ACS observations of the southern auroras. We have discussed the variety of morphologies exhibited by the northern auroras, which is broadly consistent with those observed in the south. Hence, the quiet-time oval is typically brightest on the dawnside, while during storm-time the auroras brighten and expand poleward on the dawnside before fading and rotating around to the dayside. Particularly prominent during the program were poleward forms near noon, likely associated with reconnection with the B_y-dominated IMF. We also observed main oval features associated with double sheets of field-aligned current in the outer magnetosphere, and transient forms on the duskside.

In order to compare the location of the auroras in both hemispheres, we have first obtained the statistical location of the southern auroras as observed during a large HST/ACS program which executed in 2007/2008. Our new southern boundary locations, determined by fitting Gaussians plus quadratic backgrounds to meridional cuts, have overall mean co-latitudes of ∼ 17.4° ± 1.9° and ∼ 13.5° ± 3.4° for the equatorward and poleward boundaries, respectively, and are broadly consistent with the previous boundary locations determined by Badman et al. (2006), although with smaller uncertainty owing to the larger data set employed here. Our boundaries do, however, exhibit consistent ∼1–1.5° equatorward offsets from those of Badman et al. (2006) on the dawnside, and a ∼2° poleward displacement of the poleward boundary on the dusk side. Compared to Carbary's (2012) boundaries, our

equatorward boundary lies consistently ~1° poleward, and the poleward boundary is located ~2° equatorward, i.e. in between the boundaries of Badman et al. (2006) and Carbary (2012).

For the northern auroras, we determined mean co-latitudes of ~14.6° ± 2.3° and ~10.3° ± 2.3° for the equatorward and poleward boundaries, respectively. At LTs earlier than ~10–11 h, our northern boundaries are broadly consistent with the southern boundaries mapped along magnetic field lines into the northern ionosphere and, in the case of the equatorward boundary, with the mean circle fit to the IR auroras, which are all ~2–3° poleward of the equatorward Carbary (2012) boundary. At later local times our boundary determinations jump to ~2–5° poleward of the mapped southern, mean IR circle and Carbary (2012) boundaries, before rejoining the latter boundaries near to ~18 h LT. These modest differences between the boundaries determined using HST and Cassini UVIS, which likely arise from differences in signal-to-noise and detector sensitivity, highlights the need to exercise reasonable caution when directly comparing results obtained using the two instruments.

Using the above-determined boundary locations, we calculated a ~7 ± 18 GWb difference between the flux enclosed within the mean co-latitudes of the southern and northern equatorward boundaries, as determined using the 'Cassini 5' magnetic field model of Cao et al. (2012). Whilst consistent with zero, the difference was large enough to induce further examination, such that, following Nichols et al. (2008), we fitted circles to the equatorward boundaries of the quiet-time auroras in order to remove any effects due to auroral storms, poleward dayside reconnection-induced forms, or the planetary period oval oscillation. The mean radii of ~17.8° and ~16.3° correspond to a difference in encircled magnetic flux of ~2 ± 18 GWb, i.e. consistent with zero. The implication is that the more poleward locations of our northern boundaries are due to an increased presence of poleward forms in the noon and afternoon sector such as that in e.g. Fig. 1 during the northern observations, rather than a significant inaccuracy at ionospheric altitudes in magnetic field models. However, magnetic field measurements during the upcoming proximal orbits at the end phase of the Cassini mission will provide an opportunity to test this conjecture. The 2007–2008 southern observations were obtained during the deep Solar Minimum which comprised the declining phase of Solar Cycle 23 the start of Solar Cycle 24, while the 2011–2013 observations occurred during the rising phase to near-Maximum of Solar Cycle 24. Such an increased prevalence of poleward forms, generally associated with the solar wind interaction, thus possibly originates from the difference in Solar Cycle phase in which the northern and southern observations were executed, although as discussed by Jackman and Arridge (2011), the Solar Cycle modulation of the driving of giant planet magnetospheres is likely to be more complicated than a simple variation of the dayside reconnection voltage.

We have also considered the modulation of the northern auroral location and intensity by magnetic PPO phase. We showed that the centre coordinates from circle fits to the quiet-time ovals vary roughly sinusoidally with the northern PPO phase. The phasing of the oval oscillation, with maximum duskward displacement at $\phi_{mag\,N} \simeq 131° \pm 5°$, was essentially midway between the $\Psi_{mag\,N} = 90°$ and 180° expectations for the rotating effective dipole and the offset of field-aligned current signatures, respectively. Hence, according to these data neither of these effects dominate the oscillation phase of the northern oval. The overall motion of the oval with the northern PPO phase was that of an elongated ellipse with semi-major axis of ~1.6 ± 0.2°, i.e. consistent with that previously observed for the southern oval, although the ellipse for the north was orientated more toward the dawn–dusk meridian than for the south. However, a caveat to this is that the noon-midnight motion is not very well constrained since the night side oval is off the limb of the planet in these observations. Further HST observations as the planet moves toward northern summer and the oval becomes fully visible on the planet's disk are therefore highly desirable, in order to constrain the oval rotation fully.

We further showed that the intensity of the northern auroras was modulated by PPO phase, although the behaviour is not as straightforward as is the case for the south. There is some evidence of modulation near $\phi_{mag\,N} = 0°$ at dawn, consistent with the expectations based on analogy with the south and the northern PPO current system, but there were also enhancements at phases not easily explained by the northern PPO phase. We did not obtain quiet-time images at phase $\phi_{mag\,S} = 0°$ during intervals where a southern PPO signal is present in the magnetosphere, such that we cannot state whether a similar enhancement occurs for this system. There is some weak evidence that suggests the existence of emission which appears fixed around $\Psi_{mag\,S} = 90°$, which would be associated with secondary inter-hemispheric currents originating from the southern PPO current system, although this result is not particularly robust as it relies heavily on data obtained in 2012, when the southern PPO signal was not present in the magnetosphere.

We finally examined the co-added auroral emission in frames which corotate with the PPO current systems. To place the northern results in context, we first examined in this manner the southern auroras observed in 2007–2008, and showed that enhancements in intensity occur near $\Psi_{mag\,S} = 270°$, i.e. consistent with the expectation on the basis of the previous analyses, and the southern PPO current system, although only weak, if any, enhancements were observed at $\Psi_{mag\,N} = 270°$, such that in these images there is little evidence of any modulation owing to secondary inter-hemispheric currents associated with the northern PPO current system. On the other hand, it is possible that the emission observed near $\Psi_{mag\,N} = 90°$ implies the existence of a reversed current system compared with the expectation for inter-hemispheric currents. For the northern images, there is emission near $\Psi_{mag\,N} = 90°$ for 2011 and 2012, although in the case of the former the emission region is fairly broad, while for the latter the emission is not overly bright. There is no bright emission near $\Psi_{mag\,N} = 90°$ in the 2013 data, and instead brightening near to $\Psi_{mag\,N} = 270°$ could again imply the opposite sense of currents. Similarly for the southern PPO phase, there is again some apparent evidence for emission near $\Psi_{mag\,S} = 90°$ during 2011 and 2012, i.e. which would be consistent with modulation by inter-hemispheric secondary currents originating from the southern PPO currents, although we recall the important caveats for the southern PPO phases discussed above. To summarise, then, while the modulation of the southern auroras with southern PPO phase is clear, the results for the northern are not quite so clear cut, with some years indicating modulation by PPO phase and none at other times (although these changes in behaviour are not obviously coincident with the changes observed in the magnetometer data). This variability perhaps explains the overall constancy in the statistical intensity of the northern auroras observed by Carbary (2013). The progression toward northern kronian summer, along with further inclined and proximal orbits as the Cassini mission draws to an end, will perhaps shed more light on this behaviour.

Acknowledgments

Appendix A. Comments on circle fitting

In this study, the Gaussians and circles are fitted using Levenberg–Marquardt least-squares minimisation; specifically, employing the widely-used and well-tested MPFIT library (Markwardt, 2009) based on the MINPACK algorithm (Moré, 1978). The uncertainty in the coordinates of the boundary points (calculated in each case from the root-sum-square of the uncertainties in the Gaussian profile centre and FWHM, equal to $\sim$0.03° in the example shown in Fig. 3b), is roughly an order of magnitude less than the actual deviation of the auroral boundary locations from a true circle. The latter is dependent on the morphology of the auroras in each image, and is not known a priori. The uncertainties in the centre coordinates of the fitted circles are therefore determined instead by scaling the formal $1 - \sigma$ errors returned by the function by the mean deviation of the boundary points from the fitted circle. Results applying this procedure to simulated noisy and incomplete data are shown in Fig. 13. Simulated data are shown in the top panels of Fig. 13. In each case eight points are randomly distributed over an incomplete azimuthal range, with random radial deviations of $\sim$0.5° (left) and $\sim$1.5° (right) from a 15° circle centred on the origin. The 'true' circle is shown in red, with the fitted circle shown in blue. The centre of the circle is shown by the blue cross, with the length of the arms of the cross indicating the uncertainties in each direction. The $\sim$0.5° case is representative of the actual deviations in auroral images, while the $\sim$1.5° case is provided such that the deviations from the centre can be easily visualised. The circle centres in these cases are determined to be $(x, y) = (-0.45 \pm 0.78, -0.09 \pm 0.30)$ for the $\sim$0.5° case and $(x, y) = (-0.99 \pm 1.53, 0.90 \pm 0.86)$ for the $\sim$1.5° case, i.e. in each case essentially consistent with the 'true' value of $(x, y) = (0, 0)$ (note x and y are plotted in the form used in the main body of the paper, i.e. x positive toward the bottom, and y positive toward the right). In each case the uncertainty in the x direction is larger than the y direction, owing to the incomplete azimuthal distribution of the simulated data, which roughly simulates the case for the auroral images. In order to indicate that such errors are reasonable, we show results from 100 such fits in each case, with the circle centres shown by blue dots, and the red crosses centred on the origin indicating mean uncertainty values obtained in the fits. The mean errors are consistent with the spread of the centre values, and are thus representative of the uncertainty of each fit.

Appendix B. Supplementary material

Supplementary data associated with this article can be found, in the online version, at http://dx.doi.org/10.1016/j.icarus.2015.09.008.

References

Andrews, D.J. et al., 2010. Magnetospheric period oscillations in Saturn's magnetosphere: Comparison of equatorial and high-latitude magnetic field periods with north and south SKR periods. J. Geophys. Res. 115 (A12), <http://doi.wiley.com/10.1029/2010JA015666> A12252.

Andrews, D.J. et al., 2011. Planetary period oscillations in Saturn's magnetosphere: Evidence in magnetic field phase data for rotational modulation of Saturn kilometric radiation emissions. J. Geophys. Res. 116 (A9), http://dx.doi.org/10.1029/2011JA016636 A09206.

Andrews, D.J. et al., 2012. Planetary period oscillations in Saturn's magnetosphere: Evolution of magnetic oscillation properties from southern summer to post-equinox. J. Geophys. Res. 117 (A4), http://dx.doi.org/10.1029/2011JA017444 A04224.

Badman, S.V. et al., 2006. A statistical analysis of the location and width of Saturn's southern auroras. Ann. Geophys. 24 (12), 3533–3545, <http://gateway.isiknowledge.com/gateway/Gateway.cgi?GWVersion=2&SrcAuth=Alerting&SrcApp=Alerting&DestApp=WOS&DestLinkType=FullRecord;KeyUT=000244147900029>.

Badman, S.V. et al., 2011. Location of Saturn's northern infrared aurora determined from Cassini VIMS images. Geophys. Res. Lett. 38 (3), n/a–n/a <http://doi.wiley.com/10.1029/2010GL046193>.

Badman, S.V. et al., 2012a. Cassini observations of ion and electron beams at Saturn and their relationship to infrared auroral arcs. J. Geophys. Res. 117 (A1), n/a–n/a, http://dx.doi.org/10.1029/2011JA017222.

Badman, S.V. et al., 2012b. Rotational modulation and local time dependence of Saturn's infrared H_3^+ auroral intensity. J. Geophys. Res. 117 (A9), http://dx.doi.org/10.1029/2012JA017990 A09228.

Bunce, E.J. et al., 2014. Cassini nightside observations of the oscillatory motion of Saturn's northern auroral oval. J. Geophys. Res. 119 (5), 3528–3543, http://dx.doi.org/10.1002/2013JA019527.

Bunce, E.J., Cowley, S.W.H., Milan, S.E., 2005. Interplanetary magnetic field control of Saturn's polar cusp dynamics. Ann. Geophys. 23 (4), 1405–1431, http://dx.doi.org/10.5194/angeo-23-1405-2005.

Cao, H. et al., 2012. Saturns high degree magnetic moments: Evidence for a unique planetary dynamo. Icarus 221 (1), 388–394, http://dx.doi.org/10.1016/j.icarus.2012.08.007.

Carbary, J.F., 2012. The morphology of Saturn's ultraviolet aurora. J. Geophys. Res. 117 (A6), http://dx.doi.org/10.1029/2012JA017670 A06210.

Carbary, J.F., 2013. Longitude dependences of Saturn's ultraviolet aurora. Geophys. Res. Lett. 40 (10), 1902–1906, http://dx.doi.org/10.1002/grl.50430.

Carbary, J.F., Mitchell, D.G., 2013. Periodicities in Saturn's magnetosphere. Rev. Geophys. 51 (1), 1–30, http://dx.doi.org/10.1002/rog.20006.

Clarke, J.T. et al., 2005. Morphological differences between Saturn's ultraviolet aurorae and those of Earth and Jupiter. Nature 433 (7027), 717–719.

Clarke, J.T. et al., 2009. Response of Jupiter's and Saturn's auroral activity to the solar wind. J. Geophys. Res. 114 (A), <http://adsabs.harvard.edu/cgi-bin/nph-data_query?bibcode=2009JGRA..114.5210C&link_type=EJOURNAL> A05210.

Cowley, S.W.H. et al., 2005. Reconnection in a rotation-dominated magnetosphere and its relation to Saturn's auroral dynamics. J. Geophys. Res. 110 (A2), <http://onlinelibrary.wiley.com.ezproxy3.lib.le.ac.uk/doi/10.1029/2004JA010796/full> A02201.

Crary, F.J. et al., 2005. Solar wind dynamic pressure and electric field as the main factors controlling Saturn's aurorae. Nature 433 (7027), 720–722.

Dougherty, M.K. et al., 2005. Cassini magnetometer observations during Saturn orbit insertion. Science 307 (5713), 1266–1270, http://dx.doi.org/10.1126/science.1106098.

Gérard, J.-C. et al., 2004. Characteristics of Saturn's FUV aurora observed with the Space Telescope Imaging Spectrograph. J. Geophys. Res. 109 (A18), http://dx.doi.org/10.1029/2004JA010513 A09207.

Gérard, J.-C. et al., 2005. Signature of Saturn's auroral cusp: Simultaneous Hubble Space Telescope FUV observations and upstream solar wind monitoring. J. Geophys. Res. 110 (A9), http://dx.doi.org/10.1029/2005JA011094 A11201.

Gérard, J.-C. et al., 2009. Altitude of Saturn's aurora and its implications for the characteristic energy of precipitated electrons. Geophys. Res. Lett. 36 (2), n/a–n/a <http://gateway.isiknowledge.com/gateway/Gateway.cgi?GWVersion=2&SrcAuth=Alerting&SrcApp=Alerting&DestApp=WOS&DestLinkType=FullRecord;KeyUT=000262747700005>.

Grodent, D. et al., 2005. Variable morphology of Saturn's southern ultraviolet aurora. J. Geophys. Res. 110 (A9), http://dx.doi.org/10.1029/2004JA010983 A07215.

Grodent, D. et al., 2010. On the origin of Saturn's outer auroral emission. J. Geophys. Res. 115 (A8), <http://doi.wiley.com/10.1029/2009JA014901> A08219.

Grodent, D. et al., 2011. Small-scale structures in Saturn's ultraviolet aurora. J. Geophys. Res. 116 (A9), http://dx.doi.org/10.1029/2011JA016818 A09225.

Gurnett, D.A. et al., 2009. Discovery of a north–south asymmetry in Saturn's radio rotation period. Geophys. Res. Lett. 36 (16), http://dx.doi.org/10.1029/2009GL039621 L16102.

Gurnett, D.A. et al., 2011. The rotation of plasma at high latitudes in Saturn's magnetosphere and its relation to the eccentric rotation of the northern and southern auroral ovals. Geophys. Res. Lett. 38 (21), n/a–n/a <http://doi.wiley.com/10.1029/2011GL049547>.

Gustin, J. et al., 2012. Conversion from HST ACS and STIS auroral counts into brightness, precipitated power, and radiated power for H_2 giant planets. J. Geophys. Res. 117 (A7), <http://ws.isiknowledge.com/cps/openurl/service?url_ver=Z39.88-2004&rft_id=info:ut/000306910600001> A07316.

Hunt, G.J. et al., 2014. Field-aligned currents in Saturn's southern nightside magnetosphere: Subcorotation and planetary period oscillation components. J. Geophys. Res. 119 (1), 9847–9899, <http://adsabs.harvard.edu/cgi-bin/nph-data_query?bibcode=2014JGRA..119.9847H&link_type=EJOURNAL>.

Jackman, C.M. et al., 2013. Auroral counterpart of magnetic field dipolarizations in Saturn's tail. Planet. Space Sci., 34–42, http://dxdoi.org/10.1016/j.pss.2013.03.010.

Jackman, C.M., Arridge, C.S., 2011. Solar cycle effects on the dynamics of Jupiters and Saturns magnetospheres. Solar Phys. 274 (1-2), 481–502, http://dx.doi.org/10.1007/s11207-011-9748-z.

Kurth, W.S. et al., 2007. A Saturnian longitude system based on a variable kilometric radiation period. Geophys. Res. Lett. 34 (2), http://dx.doi.org/10.1029/2006GL028336 L02201.

Kurth, W.S. et al., 2008. An update to a saturnian longitude system based on kilometric radio emissions. J. Geophys. Res. 113 (A12), http://dx.doi.org/10.1029/2007JA012861 A05222.

Lamy, L. et al., 2009. An auroral oval at the footprint of Saturn's radiosources, colocated with the UV aurorae. J. Geophys. Res. 114 (A10), <http://doi.wiley.com/10.1029/2009JA014401> A10212.

Lamy, L., 2011. Variability of southern and northern SKR periodicities. In: Rucker, H. O. (Ed.), Proceedings of the Seventh International Workshop on Planetary, Solar, and Heliospheric Radio Emissions. Austrian Acad. Sci., Vienna, pp. 39–50 <http://hw.oeaw.ac.at?arp=0x002a1cf7>.

Lamy, L. et al., 2013. Multispectral simultaneous diagnosis of Saturn's aurorae throughout a planetary rotation. J. Geophys. Res. 118 (8), 4817–4843, http://dx.doi.org/10.1002/jgra.50404.

Markwardt, C.B., 2009. Non-linear least squares fitting in IDL with MPFIT. In: Bohlender, D.A., Dowwler, P., Durand, D. (Eds.), Astronomical Data Analysis Software and Systems XVIII. Quebec, pp. 251–254.

Meredith, C.J. et al., 2013. Simultaneous conjugate observations of small-scale structures in Saturn's dayside ultraviolet auroras – Implications for physical origins. J. Geophys. Res. 118 (5), 2244–2266, http://dx.doi.org/10.1002/jgra.50270.

Meredith, C.J. et al., 2014. Saturn's dayside ultraviolet auroras: Evidence for morphological dependence on the direction of the upstream interplanetary magnetic field. J. Geophys. Res. 119 (3), 1994–2008, <http://adsabs.harvard.edu/cgi-bin/nph-data_query?bibcode=2014JGRA..119.1994M&link_type=EJOURNAL>.

Mitchell, D.G. et al., 2009. Recurrent energization of plasma in the midnight-to-dawn quadrant of Saturn's magnetosphere, and its relationship to auroral UV and radio emissions. Planet. Space Sci. 57 (14–15), 1732–1742, <http://linkinghub.elsevier.com/retrieve/pii/S0032063309001044>.

Moré, J.J., 1978. The Levenberg–Marquardt algorithm: Implementation and theory. In: Numerical Analysis. Springer, Berlin Heidelberg, pp. 105–116, <http://www.springerlink.com/index/10.1007/BFb0067700>.

Nichols, J.D. et al., 2008. Oscillation of Saturn's southern auroral oval. J. Geophys. Res. 113 (A11), http://dx.doi.org/10.1029/2008JA013444 A11205.

Nichols, J.D. et al., 2009. Saturn's equinoctial auroras. Geophys. Res. Lett. 36 (24), http://dx.doi.org/10.1029/2009GL041491 L24102.

Nichols, J.D. et al., 2010a. Variation of Saturn's UV aurora with SKR phase. Geophys. Res. Lett. 37 (15), n/a–n/a <http://doi.wiley.com/10.1029/2010GL044057>.

Nichols, J.D. et al., 2014. Dynamic auroral storms on Saturn as observed by the Hubble Space Telescope. Geophys. Res. Lett. 41 (10), 3323–3330, http://dx.doi.org/10.1002/2014GL060186.

Nichols, J.D., Cowley, S.W.H., Lamy, L., 2010b. Dawn–dusk oscillation of Saturn's conjugate auroral ovals. Geophys. Res. Lett. 37 (24), n/a–n/a <http://doi.wiley.com/10.1029/2010GL045818>.

Provan, G. et al., 2011. Magnetospheric period magnetic field oscillations at Saturn: Equatorial phase jitter produced by superposition of southern and northern period oscillations. J. Geophys. Res. 116 (A4), http://dx.doi.org/10.1029/2011JA016827 A11205.

Provan, G. et al., 2013. Planetary period magnetic field oscillations in Saturn's magnetosphere: Postequinox abrupt nonmonotonic transitions to northern system dominance. J. Geophys. Res. 118 (6), 3243–3264, http://dx.doi.org/10.1002/jgra.50186.

Provan, G., Cowley, S.W.H., Nichols, J.D., 2009. Phase relation of planetary-period oscillations of Saturn's auroral oval and equatorial magnetospheric magnetic field. J. Geophys. Res. 114 (A4), http://dx.doi.org/10.1029/2008JA013988 A04205.

Pryor, W.R. et al., 2011. The Enceladus auroral footprint at Saturn. Nature 472 (7343), 331–333, <http://www.nature.com/doifinder/10.1038/nature09928>.

Radioti, A. et al., 2009. Transient auroral features at Saturn: Signatures of energetic particle injections in the magnetosphere. J. Geophys. Res. 114 (A3), <http://doi.wiley.com/10.1029/2008JA013632> A03210.

Radioti, A. et al., 2011. Bifurcations of the main auroral ring at Saturn: Ionospheric signatures of consecutive reconnection events at the magnetopause. J. Geophys. Res. 116 (A11), http://dx.doi.org/10.1029/2011JA016661 A11209.

Radioti, A. et al., 2013. Signatures of magnetospheric injections in Saturn's aurora. J. Geophys. Res.: Space Phys. 118 (5), 1922–1933, <http://onlinelibrary.wiley.com.ezproxy4.lib.le.ac.uk/doi/10.1002/jgra.50161/full>.

Southwood, D.J., Kivelson, M.G., 2007. Saturn magnetospheric dynamics: Elucidation of a camshaft model. J. Geophys. Res. 112 (A12), http://dx.doi.org/10.1029/2007JA012254 A12222.